A Soft-Switching Secondary-Side Control Method Without AC Current Detection for Wireless Power Transfer Systems

Kangxing Zheng, Jingzhi Ren, and Wenxing Zhong, *Senior Member, IEEE*

***Abstract*—This article proposes a novel synchronous secondary-side control method for wireless power transfer (WPT) systems without AC current detection and real-time wireless communication. The proposed method includes a fast output-control loop for output control and a synchronization loop for phase synchronization and ensuring zero voltage switching of the secondary-side switches. The regulation strategy for the initial stage is designed to avoid the issue of monotonicity. The small-signal model of the WPT system with the proposed control method is derived based on the generalized state space averaging and extended describing function methods. Based on the established model, the control system is designed, and the stability of the proposed method is studied. Experimental results based on a 157 W prototype are presented to verify the effectiveness and dynamic performance of the proposed control method.**

***Index Terms*—Nonreal-time wireless communication, phase synchronization, small-signal modeling, soft switching, wireless power transfer (WPT).**

I. Introduction

THE wireless power transfer (WPT) technology has sparked widespread interest in both academic community and business domain worldwide due to its unique advantages of safety and convenience. As a result, WPT is widely used in various applications.

A typical WPT system is essentially a resonant DC–DC converter, with two major differences. One is the magnetic coupling which is usually much weaker than an insulation transformer, and the other is the wireless communication between the primary and secondary controllers. The commonly used wireless communication technologies may introduce a time delay in milliseconds level [1], [2], [3]. Thereby, fast response is difficult to achieve if the close-loop control of the system relies on wireless communication. To deal with this issue, the dual side active bridge control is widely used in WPT systems [4], [5], [6], [7], [8], [9], [10], [11], [12], [13], [14], [15], [16], [17], [18], [19], [20], [21], [22], [23], [24], [25], [26], [27], [28], [29].

The major challenge of the secondary-side control is the synchronization of the secondary-side driving signals with respect to the primary-side driving signals. A few techniques have been reported to deal with this issue, which are summarized as follows.

1) In [4] and [5], an auxiliary coil is adopted in the secondary side to obtain the phase information of the primary-side current. By detecting the voltage induced by the magnetic field generated by the primary-side current on the auxiliary coil, a voltage signal synchronized with the primary-side driving signals can be obtained. However, the accuracy of the synchronization signal depends on the design of the signal processing circuit and is sensitive to the system parameters. In [6] and [7], auxiliary driving coils are added to the primary side to transmit the reference phase for synchronization, but this increases the system's complexity and cost.
2) Based on the detection of the AC current or voltage, the synchronization signal can be obtained without auxiliary coils [8], [9], [10], [11], [12], [13], [14], [15], [16], [17], [18]. In [8] and [9], a synchronous control method based on the active power and reactive power measurement is employed. The sensed rectifier input current and voltage are utilized to calculate the real-time power flow with an analog processing circuit, which contains phase-shifting circuits, multipliers, and low-pass filters. Based on the principle of zero reactive power generated by the secondary rectifier, the synchronization state of the secondary control is realized. In [10], the voltage of the secondary resonant capacitor is used for frequency synchronization, while phase synchronization is performed by tracking the maximum output DC voltage. However, in high-voltage applications, this method requires reliable isolation, and resynchronization is necessary when system parameter drifts occur. In [11], [12], [13], [14], and [15], the synchronization signal is obtained through zero-crossing detection of the rectifier input current. However, synchronization methods based on detecting the rectifier input current could suffer from inaccuracies caused by current harmonics or noise, which may pose a serious challenge

Received 7 May 2024; revised 1 August 2024 and 2 October 2024; accepted 27 October 2024. Date of publication 1 November 2024; date of current version 18 December 2024. Recommended for publication by Associate Editor C. Lee. *(Corresponding author: Wenxing Zhong.)*

Kangxing Zheng is with the College of Electrical Engineering, Zhejiang University, Hangzhou 310027, China (e-mail: kxzheng@zju.edu.cn).

Jingzhi Ren is with the Douch Power Technology Ltd., Ningbo 315105, China (e-mail: renjingzhi@douchpower.com).

Wenxing Zhong is with the Faculty of Electrical Engineering and Computer Science, Ningbo University, Ningbo 315211, China (e-mail: zhongwenxing@nbu.edu.cn).

Color versions of one or more figures in this article are available at https://doi.org/10.1109/TPEL.2024.3490532.

Digital Object Identifier 10.1109/TPEL.2024.3490532

to the control stability of the system in high-frequency applications [16], [17], [18].

3) To eliminate the troubles of detecting the rectifier input current, a synchronization strategy based on the perturbation and observation (P&O) method with only DC current or voltage detection is proposed in [19], [20], and [21]. Synchronization is achieved through tracking the peak value of the output DC current or the phase-shift angle between two legs of the secondary full-bridge converter. However, the basic principle of the P&O method relies on zero reactive power generated by the secondary rectifier, which means the rectifier input voltage and input current are in phase. Thereby, zero phase angle (ZPA) is realized. When the phase-shift modulation is applied, ZPA of the rectifier might lead to hard-switching of the rectifier switches, which may reduce efficiency and cause EMI problems [22], [23], [24]. Another drawback of the P&O method is the dynamic performance, which is the common issue for control methods based on P&O. In [25], a dual-side control method is proposed that eliminates the need for synchronization. However, this method cannot achieve soft switching, and the irregular current on the primary side results in high current stress.

This article proposes a novel synchronous secondary-side control method without the detection of AC current or voltage. The duty cycle of the rectifier input voltage is regulated with a fast speed for output control. Thereby, a fast transient response is possible. On the other hand, the phases of the rectifier driving signals are adjusted with a low speed so that the rectifier input current leads the rectifier input voltage by a certain phase to realize phase synchronization and zero voltage switching (ZVS) of the switches. Only the output DC current or voltage is sensed. The proposed method can not only reduce the cost and volume of the system but also avoid the disadvantage that AC current sampling is easily disturbed by high-frequency noises. Thus, the proposed method is suitable for high-frequency applications with synchronous control.

The rest of this article is organized as follows. Section II introduces the characteristics of ZPA control and capacitive phase angle (CPA) control methods, and the strategy of the proposed CPA synchronization control method. In Section III, the monotonicity of the proposed control loops is studied and a regulation method for the initial stage is introduced. The influence of system parameter errors on the control system is analyzed. Based on the generalized state space averaging (GSSA) method, a small-signal model of the control system is built. Section IV provides the controller design process and simulation results. In Section V, experimental results are given to verify the effectiveness of the proposed method. Finally, Section VI concludes this article.

II. Characteristics of Synchronous Control Methods

A. SS WPT System

The basic circuit topology of a WPT system with series–series (SS) compensation [26] is shown in Fig. 1. In Fig. 1(a), S_1–S_4 and S_5–S_8 are the switches of the inverter and the rectifier,

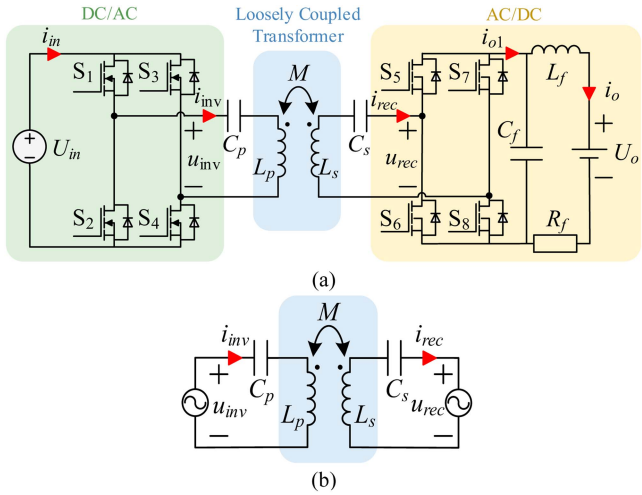

Fig. 1. (a) Basic circuit topology of SS WPT system. (b) Fundamental equivalent circuit.

respectively. L_p and L_s are the self-inductances of the primary and secondary coils, respectively. M is the mutual inductance between the two coils. C_p and C_s are the resonant capacitors. C_f and L_f are the capacitance and inductance of the output filter, respectively. U_{in} is the input DC link voltage. U_o is the charging voltage, and i_o is the charging current. u_{inv} and i_{inv} are the inverter output voltage and current, respectively, and u_{rec} and i_{rec} are the rectifier input voltage and current, respectively.

The parameters of the compensation tanks are designed with the following resonant conditions:

$$\begin{cases} \omega L_p - \frac{1}{\omega C_p} = 0 \\ \omega L_s - \frac{1}{\omega C_s} = 0 \end{cases} \tag{1}$$

where $\omega = 2\pi f_0$, and f_0 is the resonant frequency of the system. Define $T_0 = 2\pi/\omega$ as the resonant period.

B. ZPA and CPA Control Methods

Based on the criterion of whether the rectifier impedance is resistive or capacitive, the secondary phase shift control methods can be divided into two categories: ZPA control [19], [20], [21] and CPA control [23]. Fig. 2 shows the system waveforms with ZPA control and CPA control. β is the angle corresponding to the time interval when u_{rec} is 0 V. In CPA control, φ is the angle difference between P_1 and P_2, where P_1 and P_2 are the first positive zero-crossing points of i_{rec} and u_{rec}. In ZPA control, u_{rec} and i_{rec} are in phase, which leads to hard-switching of the rectifier switches, whereas CPA control is able to realize ZVS if $\varphi \geq 0$.

T_P is the period of u_{inv} and T_S is the period of u_{rec}. T_P and T_S are both set to the resonant period T_0. However, due to the slight difference of the crystal oscillator frequencies of the primary-side and secondary-side controllers, there is a tiny period difference ΔT between T_P and T_S. Without synchronization control, ΔT causes a periodic change in the output power [13]. The effect of ΔT can be eliminated by adopting a synchronous

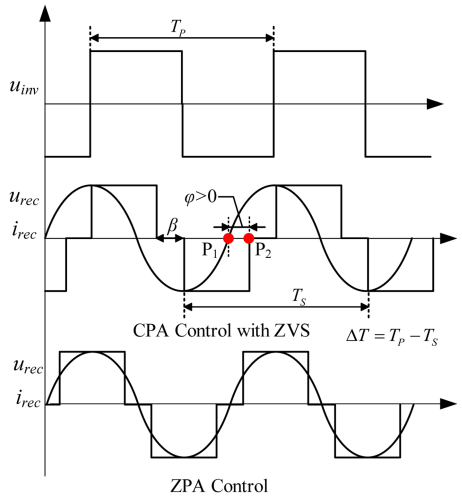

Fig. 2. System waveforms with ZPA control and CPA control.

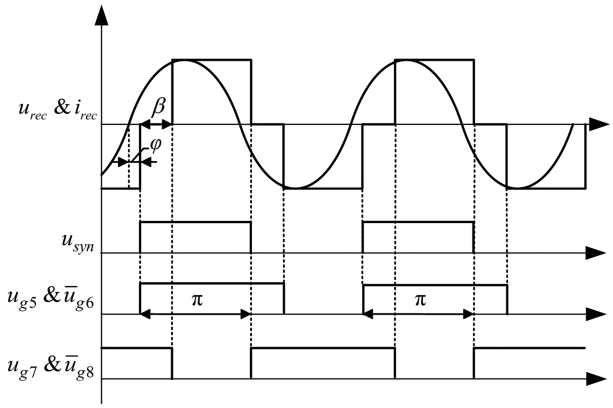

Fig. 3. Switching signals waveforms of the secondary rectifier.

control to periodically update the phases of the secondary-side driving signals with respect to the primary side.

The reported synchronous control methods without resonant current detection [19], [20], [21] adopts the P&O method to achieve phase synchronization. The method is to ensure a largest output current by using the P&O method. Therefore, it can naturally achieve ZPA but not CPA of the rectifier. More details could be found in [19], [20], and [21].

C. Principle of the Proposed CPA Synchronization Control Method Without AC Current Detection

Define $d_\beta = \beta/\pi$ $(0 < d_\beta < 1)$ as the coefficient, which is determined by the duty cycle of the rectifier voltage. Define $d_\varphi = \varphi/\pi$ as the coefficient, which is determined by the phase of the rectifier voltage. The steady-state I_o with CPA control can be calculated as

$$I_o = \frac{I_{rec}}{\pi}\left[\cos\left(d_\varphi \pi\right) + \cos\left(d_\varphi \pi + d_\beta \pi\right)\right] \tag{2}$$

where I_{rec} is the fundamental amplitude of the rectifier input current i_{rec}.

The general expression for I_{rec} with SS compensation is given by

$$I_{rec} = \frac{\omega M U_{inv}}{\sqrt{\left[\omega^2 M^2 + R_1 R_s - X_p X_s\right]^2 + \left(R_1 X_s + X_p R_s\right)^2}} \tag{3}$$

where

$$X_p = \omega L_p - \frac{1}{\omega C_p}$$

$$R_s = \frac{8}{\pi^2}\frac{U_o}{I_o}\cos^2\frac{d_\beta \pi}{2}\cos^2\left(\frac{d_\beta \pi}{2} + d_\varphi \pi\right) + R_2$$

$$X_s = -\frac{4}{\pi^2}\frac{U_o}{I_o}\cos^2\frac{d_\beta \pi}{2}\sin\left(d_\beta \pi + 2d_\varphi \pi\right) + \omega L_s - \frac{1}{\omega C_s}$$

where R_1 and R_2 are the parasitic resistance of the primary and secondary resonator, respectively, U_{inv} is the fundamental amplitude of u_{inv}, which equals $4/\pi * U_{in}$.

When the system resonates and both d_φ and d_β are 0, I_{rec} is given by

$$I_{rec} = \frac{\omega M U_{inv}\pi - 4R_1 U_o}{\omega^2 M^2 \pi + R_1 R_2 \pi}. \tag{4}$$

For a resonated WPT system with the secondary-side control, U_{inv} is considered unchanged. As both R_1 and R_2 are small, the influence of d_φ, d_β and U_o on I_{rec} can be neglected. Therefore, I_{rec} can be regarded as approximately constant in (2) and calculated using (4). In addition to the SS compensated topology, other topologies capable of making I_{rec} independent of load variations, such as the LCC–LCC compensated topology [27], are also suitable for the proposed method.

Fig. 3 shows the rectifier input voltage u_{rec}, input current i_{rec}, and the gate drive signals u_{g5}–u_{g8} for the switches of the rectifier. u_{syn} is a digital signal with a 50% duty cycle generated by the secondary controller. The gate drive signal of the high-side MOSFET S_5, i.e., u_{g5}, is triggered by the rising edge of u_{syn}. Thereby, the phase of u_{g5} is determined by u_{syn}. The gate drive signal of the other high-side MOSFET S_7, i.e., u_{g7}, lags u_{g5} by 180°. The gate drive signal of each low-side MOSFET is complement with that of the high-side MOSFET of the same leg. To create a bypass period of β, the pulse widths of u_{g5} and u_{g7}, which are with the same length, are larger than the half switching period, as shown in Fig. 3.

First, the pulse widths of u_{g5} and u_{g7} can be controlled to regulate d_β for achieving a desired output. This is the first control loop of the system, which is called the output-control loop. Then, the synchronization loop is introduced for achieving ZVS of the rectifier switches by controlling the phase of u_{syn}. The phase of i_{rec} is ideally determined by the primary-side voltage u_{inv}, which is not affected by the secondary-side control, thereby, i_{rec} can be taken as the reference for achieving a zero φ and, thus, ZVS. Ideally, if d_φ can be measured, the phase of u_{syn} can be adjusted to track a specific d_φ. However, in the proposed system, the AC current is not measured and thereby, d_φ cannot be obtained through measurements. According to (2), a zero d_φ

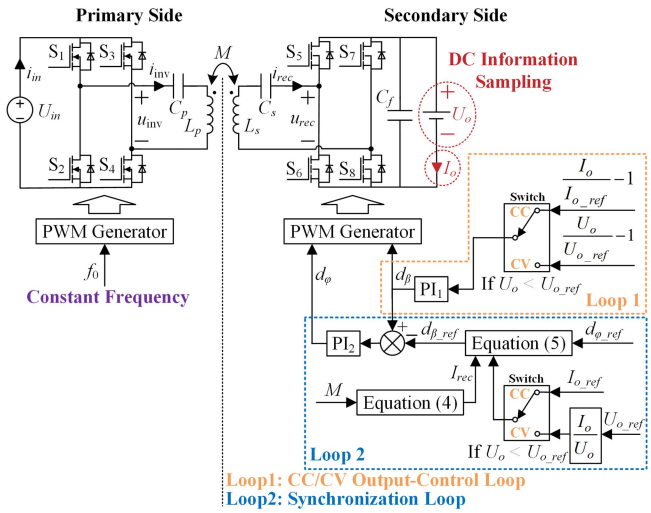

Fig. 4. Block diagram of the proposed secondary-side control method.

is corresponding to a specified value of d_β provided that I_{rec} and I_o are given. Therefore, this specified value of d_β can be used as a reference value, denoted as d_{β_ref}. If d_β at the moment equals d_{β_ref}, zero d_φ should be achieved. Otherwise, a further adjustment should be applied to the phase of u_{syn}. To eliminate interferences between two control loops, the synchronization loop is designed to be much slower than the output-control loop. This is the basic mechanism of the proposed control method without AC current detection.

Based on (2), d_{β_ref} is derived as

$$d_{\beta\_ref} = \frac{1}{\pi}\arccos\left[\frac{\pi I_{o\_ref}}{I_{rec}} - \cos\left(d_{\varphi\_ref}\pi\right)\right] - d_{\varphi\_ref}. \tag{5}$$

In the previous analysis, d_φ is assumed zero. However, to realize full ZVS in real applications, d_φ should be a bit larger than zero. In the rest of this article, d_φ is set to 0.1, which is considered as a reference d_φ and marked with d_{φ_ref}.

III. Proposed Secondary-Side Control Method

The block diagram of the proposed secondary-side control method is shown in Fig. 4. Apart from the two control loops, the mutual inductance of the system needs to be estimated for the calculation of I_{rec} and d_{β_ref}. According to [28], the mutual inductance can be estimated with DC output voltage and current. Therefore, how to extract M is not the focus of this study.

In the rest of this section, the monotonicity of the proposed control loops is first studied. Then, a regulation method for the initial stage is introduced. The influence of system parameter errors on the control system is discussed as well.

A. Output-Control Loop

The output-control loop is much faster than the synchronization loop and, thus, d_φ can be taken as a constant in every short period of time when considering the output-control loop. Thereby, the monotonicity of the output-control loop can be studied with the I_o-d_β function, as given in (2), with different values of d_φ. Taking the prototype system as an example, the specifications are given in Table I. The I_o-d_β curves are like these given in Fig. 5.

TABLE I
System Specifications and Parameters

Parameters	Values	Parameters	Values
U_{in}	380 V	U_o	52.5 V
L_p	514.9 μH	L_s	81.72 μH
C_p	6.83 nF	C_s	42.92 nF
R_1	0.98 Ω	R_2	0.11 Ω
M	72.17 μH	Air gap	60 mm
L_f	1.68 μH	C_f	95 μF
R_f	0.1 Ω	f_0	85 kHz
I_{o_ref}	3 A	d_{φ_ref}	0.1

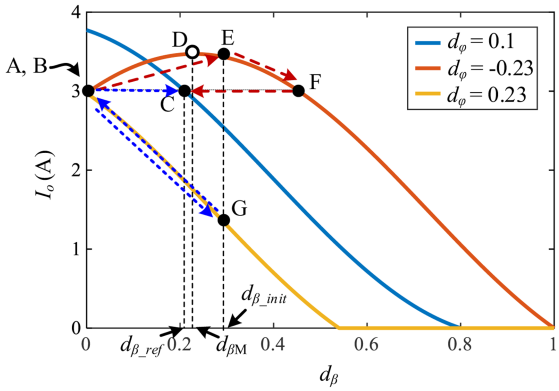

Fig. 5. I_o-d_β curves with different d_φ of the prototype system.

According to (2), $\partial I_o/\partial d_\beta$ can be calculated as

$$\frac{\partial I_o}{\partial d_\beta} = -I_{rec}\sin\left[\left(d_\beta + d_\varphi\right)\pi\right]. \tag{6}$$

Let (6) equals to 0, the value of d_β corresponding to the maximum value of I_o when $d_\varphi < 0$ is obtained as

$$d_{\beta M} = |d_\varphi|. \tag{7}$$

When $-1 < d_\varphi < 0$, $\partial I_o/\partial d_\beta$ is positive when $d_\beta < |d_\varphi|$ and negative when $d_\beta > |d_\varphi|$. Therefore, for a given negative d_φ, the I_o-d_β curve is non-monotonous within the range of [0, 1] for d_β.

When $0 < d_\varphi < 1$, $\partial I_o/\partial d_\beta$ is always negative and thereby the I_o-d_β curve is monotonous within the range of [0, 1] for d_β.

Fig. 5 shows the I_o-d_β curves with different d_φ. $d_\varphi = -0.23$ and 0.23 correspond to an output of 3 A when $d_\beta = 0$, according to (2). The desired operation point is C where $d_\beta = d_{\beta\_ref} = 0.21$ and $d_\varphi = d_{\varphi\_ref} = 0.1$. The I_o-d_β curve of $d_\varphi = -0.23$ is nonmonotonous and the peak point is located at $d_{\beta M} = 0.23$ as given by (7).

B. Synchronization Loop

On the other hand, for each given d_φ, d_β is regulated fast enough for generating the reference output. Therefore, the synchronization loop can be described by the d_β-d_φ curve with a given output, which is like the one in Fig. 6 for the prototype system.

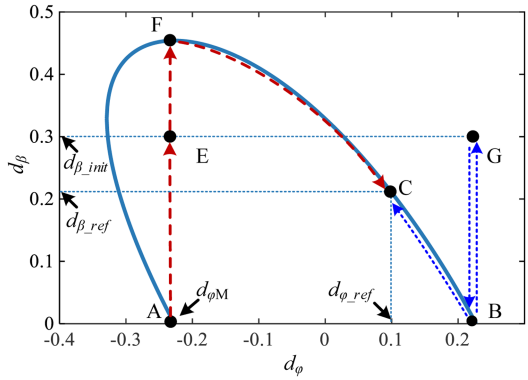

Fig. 6. d_β-d_φ curve of the prototype system when $I_o = I_{o\_ref} = 3$ A.

Similarly, based on (2), $\partial d_\beta/\partial d_\varphi$ is calculated as

$$\frac{\partial d_\beta}{\partial d_\varphi} = \frac{-\sin(d_\varphi \pi)}{\sqrt{1-\left[\cos(d_\varphi \pi) - \frac{\pi I_{o\_ref}}{I_{rec}}\right]^2}} - 1. \tag{8}$$

Let (8) equals to 0, the value of d_φ corresponding to the maximum value of d_β is obtained as

$$d_{\varphi M} = -\frac{1}{\pi}\left|\arccos\left(\frac{\pi I_{o\_ref}}{2I_{rec}}\right)\right|. \tag{9}$$

In the example system, $d_{\varphi \mathrm{M}}$ is -0.23 when $I_{o\_ref} = 3$ A.

In Fig. 6, the desired operation point is C, which is corresponding to $d_\varphi = 0.1$. Although d_φ is unknown because the AC current is not measured in the proposed system, the change in d_φ from one cycle to the next is controllable. The desired d_φ (i.e., d_{φ_ref}) is achieved by ensuring that the steady-state value of d_β tracks d_{β_ref}. The adjustment of the steady-state value of d_β is accomplished by modifying the phase variation of u_{syn} in the next cycle relative to the current cycle.

C. Initial Stage

At the initial stage, after the system is activated, the secondary gate drive signals are applied with a zero d_β, i.e., the duty cycle of the rectifier voltage is 1, and d_φ is an arbitrary value. The control loops are deactivated in this stage.

Then, d_φ is increased (or decreased) with a certain step size until the output reaches the reference. In other words, the operation points of the system for producing the reference output are located by adjusting d_φ.

For example, in Fig. 6, the operation points A or B will be found to output the reference current by adjusting d_φ when $d_\beta = 0$. It should be noted that each of the point in Fig. 6 is corresponding to the point with the same name in Fig. 5. The point A and B in Fig. 5 are the same point. Then, the two control loops are activated. The monotonicity of the output-control loop control and the synchronization loop are determined as $\partial I_o/\partial d_\beta < 0$ and $\partial d_\beta/\partial d_\varphi < 0$, respectively. To avoid monotonicity problem, an initial d_β, which is larger than $d_{\beta M}$ is applied. The initial d_β is marked as d_{β_init}, and is calculated based on (7) and (9). Starting from A or B, there are two possible paths, which are explained as follows.

1) Starting from A, i.e., $d_\varphi = -0.23$, the operation point will change to E after applying d_{β_init}, which is larger than 0.23 when $I_{o\_ref} = 3$ A. Then, it goes to F rapidly along the I_o-d_β curve of $d_\varphi = -0.23$ through the output-control loop, as shown in Fig. 5. Then, through the synchronization loop, d_φ is gradually increased and the operation point moves from F to C along the d_β-d_φ curve, as shown in Fig. 6. The complete moving paths of the operation point are given in red arrows in Figs. 5 and 6.
2) Starting from B, i.e., $d_\varphi = 0.23$, similar analysis can be performed, and the complete paths is B-G-B-C, as given in blue arrows in Figs. 5 and 6.

By applying this initial d_β, monotonicity maintains consistent for both cases.

D. Impact of Parameter Errors

Considering the parameter errors of the resonant capacitors and the mutual inductance, the calculated I_{rec}, the calculated d_{β_ref} and eventually the steady-state d_φ will deviate from their ideal values. Here error is defined as the percentage error of the actual value, with respect to the value fed into a microcontroller (MCU). Thereby, the parameter error of a capacitor due to its tolerance is given by

$$e_C = \frac{C_{act} - C_{nom}}{C_{nom}} \times 100\% \tag{10}$$

where C_{act} is the actual value of the capacitor, and C_{nom} is the nominal value of the capacitor, which resonates with the corresponding self-inductance, e_{Cp} and e_{Cs} represent the parameter errors of C_p and C_s, respectively.

The parameter error of the mutual inductance is given by

$$e_M = \frac{M_{mea} - M_{act}}{M_{act}} \times 100\% \tag{11}$$

where M_{act} is the actual mutual inductance of the windings, and M_{mea} is the measured value which is used for calculating I_{rec} and d_{β_ref}.

The analysis process of key system parameters with e_M and e_C is shown in Fig. 7. Part A involves the calculation process of the internal variables in the MCU, i.e., the calculated I_{rec} and d_{β_ref}. The former is obtained by (4); it is then used in (5) to calculate d_{β_ref} when I_{o_ref} and d_{φ_ref} are given. Since (4) and (5) does not include C_p and C_s, the calculated I_{rec} and d_{β_ref} are unaffected by e_{Cp} and e_{Cs}. d_{β_ref} is eventually used as the reference value in the phase-synchronization loop for locating d_φ to guarantee ZVS and minimal reactive power. Ideally without any parameter errors, the steady-state d_φ will equal its reference value, i.e., d_{φ_ref}, which is 0.1 in this study.

Part B involves the calculation process of the steady-state operating variables of the prototype, i.e., the steady-state I_{rec} and d_φ. The former is obtained by (3), it is then used in (2) to calculate d_φ. The steady-state output current I_o will equal I_{o_ref} with the output-control loop, and the steady-state d_β will equal d_{β_ref} with the phase-synchronization loop. As a result, the steady-state d_φ will deviate from d_{φ_ref}. The steady-state I_{rec} and d_φ are both affected by e_C and e_M based on (2) and (3).

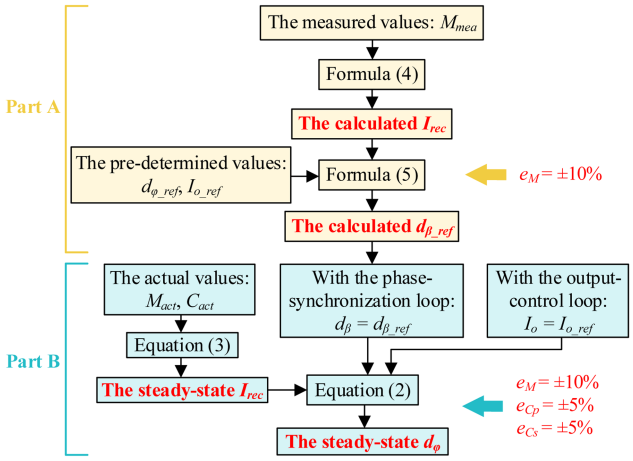

Fig. 7. Flowchart of the analysis process of key system parameters with e_M and e_C.

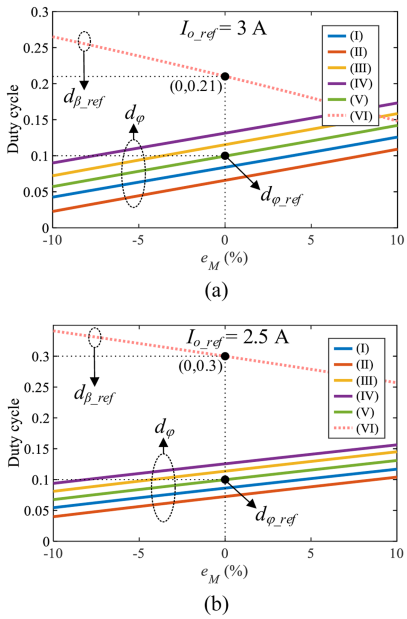

Fig. 8. Variations of the steady-state d_φ with different e_M and e_C in (I)–(V), where: (I) $e_{Cp} = 5\%$, $e_{Cs} = 5\%$; (II) $e_{Cp} = 5\%$, $e_{Cs} = -5\%$; (III) $e_{Cp} = -5\%$, $e_{Cs} = 5\%$; (IV) $e_{Cp} = -5\%$, $e_{Cs} = -5\%$; (V) $e_{Cp} = 0$, $e_{Cs} = 0$; the variations of the calculated d_{β_ref} with different e_M in (VI), for (a) $I_{o\_ref} = 3$ A and (b) $I_{o\_ref} = 2.5$ A.

Fig. 8 shows the calculated d_{β_ref} and the steady-state d_φ with different e_C and e_M, where the solid lines represent d_φ and the pink dashed line represents d_{β_ref}. The parameter errors in the primary resonant capacitor C_p, secondary resonant capacitor C_s, and mutual inductance M are considered simultaneously. In Fig. 8, C_{nom} and M_{act} are assigned by the corresponding values of C_p, C_s, and M in Table I. With zero errors, d_φ equals d_{φ_ref}, i.e., 0.1, and d_{β_ref} equals the ideal value, i.e., 0.21 for $I_{o\_ref} = 3$ A and 0.3 for $I_{o\_ref} = 2.5$ A.

In the range of ±5% errors in the value of resonant capacitors and ±10% errors in the value of mutual inductance, d_φ varies in the range of 0.02 to 0.17 and d_{β_ref} varies in the range of 0.15 to 0.27 when I_{o_ref} is 3 A. It should be noted that the constraints for the parameter errors lie in: 1) the values of d_φ should be larger than zero to realize ZVS, and 2) the value of d_{β_ref} should be larger than zero to output the required current I_{o_ref}. The entire ranges of d_φ and d_β in Fig. 8(a) are larger than zero, which means ZVS and output control can be maintained despite the parameter errors.

As shown in Fig. 8(b), when I_{o_ref} decreases from 3 A to 2.5 A, d_φ varies in the range of 0.04 to 0.16 and d_{β_ref} varies in the range of 0.26 to 0.34. Therefore, larger margins are generated with respect to zero. This implies that larger parameter errors can be tolerated if I_{o_ref} is set to a lower value.

IV. Control System Design

The proposed control method can achieve CC or CV output through the control of the proposed two loops. Based on the GSSA method [30], A small signal model of the control system is established in order to verify its stability. The detailed calculation process is provided in the Appendix. The closed loop control diagram can be summarized as Fig. 9, where the following conditions hold:

$G_{d\varphi}$: open-loop transfer function between $\hat{d}_\varphi$ and $\hat{i}_o$;
$G_{d\beta}$: open-loop transfer function between $\hat{d}_\beta$and $\hat{i}_o$;
$G_{d\varphi\beta}$: open-loop transfer function between $\hat{d}_\varphi$and $\hat{d}_{\beta\_ss}$.

For a variable x, $\hat{x}$ represents its small-signal perturbation. The steady-state duty cycle d_β is marked as d_{β_ss}. The U_o and I_o are sampled as the inputs of the fast output-control loop, and d_β is regulated to make U_o or I_o follow the reference value. In the slow synchronization loop, d_φ is adjusted to make d_β follow d_{β_ref}, thus, d_φ will be kept at d_{φ_ref}. According to (5), the value of K_1 and K_2 are expressed as

$$\begin{cases} K_1 = \dfrac{\partial d_{\beta\_ref}}{\partial d_{\varphi\_ref}} \\ K_2 = \dfrac{\partial d_{\beta\_ref}}{\partial I_{o\_ref}} \end{cases}. \tag{12}$$

The phase perturbation caused by the frequency difference between the primary and secondary controller is regarded as $\hat{d}_{\varphi p}$. The perturbation $\hat{i}_o$ is caused by the perturbation $\hat{i}_{o\_ref}$, $\hat{d}_{\varphi\_ref}$, and $\hat{d}_{\varphi p}$. As a result, $\hat{i}_o$ can be expressed as

$$\hat{i}_o = H_{i_{o\_ref}}\hat{i}_{o\_ref} + H_{d_{\varphi\_ref}}\hat{d}_{\varphi\_ref} + H_{d_{\varphi p}}\hat{d}_{\varphi p} \tag{13}$$

where

H_{io_ref} : closed-loop transfer function between $\hat{i}_{o_ref}$and $\hat{i}_o$;
$H_{d\varphi\_ref}$: closed-loop transfer function between $\hat{d}_{\varphi_ref}$and $\hat{i}_o$;
$H_{d\varphi p}$: closed-loop transfer function between $\hat{d}_{\varphi p}$and $\hat{i}_o$.

According to Fig. 9, the closed-loop transfer functions in (13) can be expressed as

$$\begin{cases} H_{i_{o\_ref}} = \dfrac{DC_1 * G_{d_\beta}}{DC_1 * G_{d_\beta} - 1} - \dfrac{DC_2 * G_{d_\varphi} * K_2}{(DC_1 * G_{d_\beta} - 1)(DC_2 * G_{d_{\varphi\beta}} - 1)} \\ H_{d_{\varphi p}} = \dfrac{G_{d_\varphi}}{(DC_1 * G_{d_\beta} - 1)(DC_2 * G_{d_{\varphi\beta}} - 1)} \\ H_{d_{\varphi\_ref}} = \dfrac{-DC_2 * G_{d_\varphi} * K_1}{(DC_1 * G_{d_\beta} - 1)(DC_2 * G_{d_{\varphi\beta}} - 1)} \end{cases} \tag{14}$$

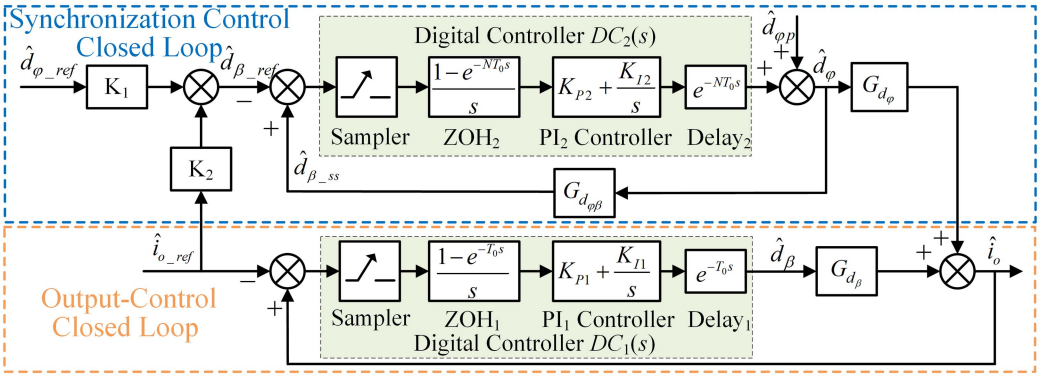

Fig. 9. Closed-loop control diagram.

where

$$DC_1(s)=\frac{1-e^{-T_cs}}{T_cs}\left(K_{P1}+\frac{K_{I1}}{s}\right)e^{-T_cs}$$

$$DC_2(s)=\frac{1-e^{-NT_cs}}{NT_cs}\left(K_{P2}+\frac{K_{I2}}{s}\right)e^{-NT_cs}$$

where T_c is the period of the output-control loop, which equals the resonant period T_0.

The exponential term $e^{-\tau s}$ is simplified using the first-order Padé approximation [31], which can be expressed as

$$e^{-\tau s}=\frac{1-\frac{\tau}{2}s}{1+\frac{\tau}{2}s}. \tag{15}$$

In the output-control loop, a PI controller is employed to make the output current track its reference value quickly. Therefore, the PI controller parameters (K_{P1}, K_{I1}) need to be designed appropriately to improve the reference tracking performance, as demonstrated by its open-loop transfer function $G_1(s)$. As shown in Fig. 9, $G_1(s) = -G_{d\beta}(s)*DC_1(s)$.

Generally, the open-loop transfer function has four indexes to assess the performance of its closed-loop control system, which are gain margin K_g, phase margin γ, low-frequency magnitude $G_1(j1)$ and cutoff frequency ω_c. In order to guarantee the stability of the control system, K_g and γ should be both positive and large enough. A sufficiently large $G_1(j1)$ and ω_c are beneficial to improve the dynamic response performance of the system.

The performance indexes of $G_1(s)$ at different values of K_{P1} and K_{I1} are calculated and given in Fig. 10, based on the small signal model in Section IV. As K_{I1} increases, K_g and γ remain basically unchanged at first and then drop rapidly, while $G_1(j1)$ and ω_c increase rapidly. As K_{P1} increases, K_g decreases and γ increases, while $G_1(j1)$ and ω_c remain unchanged. Taking into account the aforementioned calculations and analysis results, the values of K_{P1} and K_{I1} are selected as 0.007 and 50.

In the synchronization loop, the control period of the digital controller is N times longer than that of the output-control loop to ensure that the output-control loop reaches steady state within each control period of the synchronization loop. Because $\hat{d}_{\varphi p}$ and $\hat{d}_{\varphi}$ are both tiny, the resulting output current disturbance $\hat{i}_o$ can be quickly eliminated by the output-control loop. The value

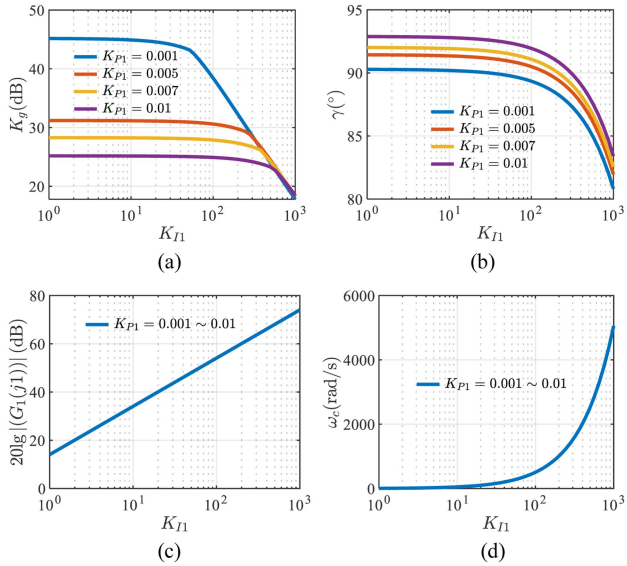

Fig. 10. Performance indexes of $G_1(s)$ at different values of K_{P1} and K_{I1} including (a) gain margin K_g, (b) phase margin γ, (c) low-frequency magnitude $G_1(j\omega)$ when $\omega = 10^0$ rad/s, and (d) cutoff frequency ω_c.

of N is set to 15 in this article, further analysis on the selection of N is provided in Section VI. The open-loop transfer function of the synchronization loop is defined as $G_2(s)$. As shown in Fig. 9, $G_2(s) = -G_{d\varphi\beta}(s) *DC_2(s)$.

The performance indexes of $G_2(s)$ at different values of K_{P2} and K_{I2} are calculated and shown in Fig. 11. As can be seen from Fig. 11, as K_{P2} increases, K_g decreases, γ and $G_2(j1)$ increases, while ω_c remains unchanged. As K_{I2} increases, K_g and γ remain unchanged, while $G_2(j1)$ and ω_c increase rapidly. In the synchronization loop, the selection of the PI controller parameters favors stability over the speed of the dynamic response, as a result, the values of K_{P2} and K_{I2} are selected as 0.02 and 0.2. The bode plots of $G_1(j\omega)$ and $G_2(j\omega)$ with the designed PI parameters are illustrated in Fig. 12.

Taking the following two cases as an example:

1) $K_{P1} = 0.007$, $K_{I1} = 50$, $K_{P2} = 0.02$, $K_{I2} = 0.2$;
2) $K_{P1} = 0.2$, $K_{I1} = 50$, $K_{P2} = 0.02$, $K_{I2} = 0.2$.

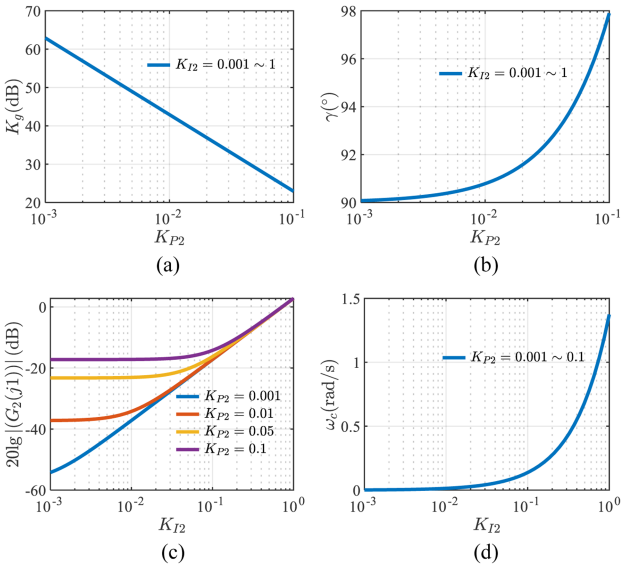

Fig. 11. Performance indexes of $G_2(s)$ at different values of K_{P2} and K_{I2} including (a) gain margin K_g, (b) phase margin γ, (c) low-frequency magnitude $G_2(j\omega)$ when $\omega = 10^0$ rad/s, and (d) cutoff frequency ω_c.

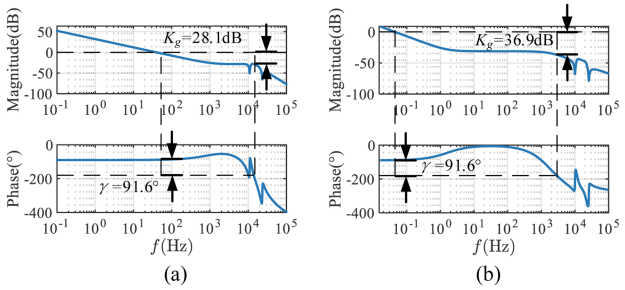

Fig. 12. Bode plots of (a) $G_1(j\omega)$ and (b) $G_2(j\omega)$ with the designed PI parameters.

According to (14), the poles of H_{io_ref} contain the poles of $H_{d\varphi\_ref}$ and $H_{d\varphi p}$. Therefore, the stability of the control system can be judged by the pole distribution of H_{io_ref}. The zero-pole distribution diagram of H_{io_ref} can be obtained based on the small-signal model, as shown in Fig. 13. The simulation waveforms using the PI parameters of the above cases are shown in Fig. 14.

As shown in Fig. 13, all the poles of H_{io_ref} have negative real parts in the first case, while in the second case there is a pair of complex conjugated poles with positive real parts. As a result, only the first case is stable. As shown in Fig. 14, the output voltage and current and PI controller outputs are stable when the system model is stable. When the system model is unstable, the output of the PI controller oscillates and cannot be stabilized at the steady-state operating point. As a result, the output voltage and current are also oscillating. The simulation results are consistent with the theoretical analysis.

V. Experimental Results

A prototype based on the structure shown in Fig. 1 is built for experiments. The inverter has two operating modes, full-bridge

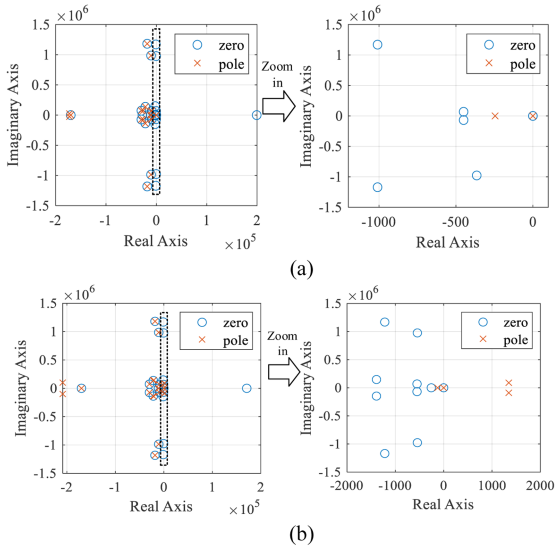

Fig. 13. Zero-pole distribution diagram of H_{io_ref} when (a) $K_{P1} = 0.007$, $K_{I1} = 50$, $K_{P2} = 0.02$, $K_{I2} = 0.2$; (b) $K_{P1} = 0.2$, $K_{I1} = 50$, $K_{P2} = 0.02$, $K_{I2} = 0.2$.

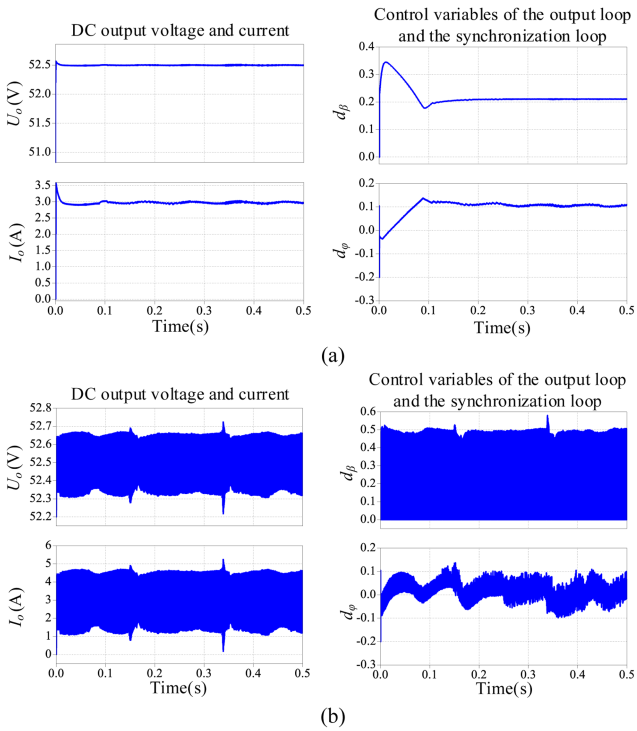

Fig. 14. Simulation waveforms when (a) $K_{P1} = 0.007$, $K_{I1} = 50$, $K_{P2} = 0.02$, $K_{I2} = 0.2$; (b) $K_{P1} = 0.2$, $K_{I1} = 50$, $K_{P2} = 0.02$, $K_{I2} = 0.2$.

(FB) and half-bridge (HB) modes, and the proposed method is applicable to each mode. The DC input voltage U_{in} is 190 V in FB mode and 380 V in HB mode. The interrupt frequency of the MCU is set to 85 kHz, which is also the control frequency of the output-control loop. The control frequency of the synchronous loop is set to 1/N of the output-control loop, where N is 15 in this article. The load is a 48 V 65 Ah lead-acid battery. The CC

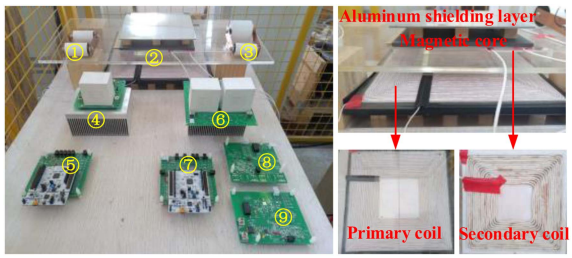

Fig. 15. Experimental prototype (① primary resonant capacitor ② coupling coils ③ secondary resonant capacitor ④ inverter ⑤ primary controller ⑥ rectifier ⑦ secondary controller ⑧ DC voltage sensing board ⑨ DC current sensing board).

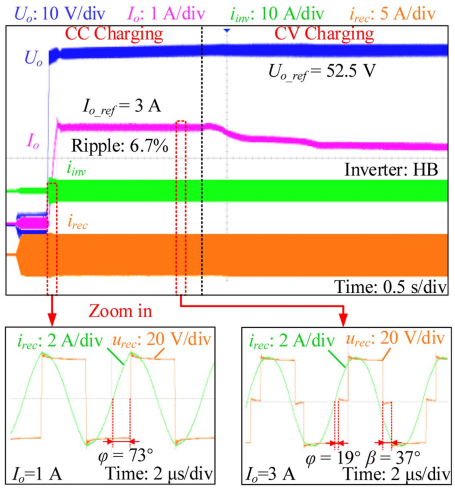

Fig. 16. Experimental waveforms during CC and CV charging with the proposed control method.

charging current is set to 3 A and the CV charging voltage is set to 52.5 V. The prototype is shown in Fig. 15 and the key parameters are given in Table I.

In this prototype, d_{φ_ref} is set to 0.1, which means the reference value of φ is 18°. d_{β_ref} is calculated as 0.21 based on (5), which means the reference value of β is 38°. Fig. 16 shows the experimental waveforms with the proposed control method. The initial battery voltage is purposely set at a high value so that the time span of CC mode is shortened.

At the initial stage, d_β is set to 0, which means β is 0°. I_o increases as d_φ gradually varies sinusoidally [13]. φ is 73° when $I_o = 1$ A as shown in Fig. 16. When I_o reaches 3 A, d_β is set to d_{β_init}, which is 0.23 based on (7) and (9), and then the synchronization and output-control loops are both activated. In the steady stage, I_o remains nearly constant at 3 A, β remains nearly constant at 37°, and φ remains nearly constant at 19°, all of which are close to their reference values. After the battery voltage increases to the reference value, the CC mode ends and the CV mode starts. As can be seen in Fig. 16, ZVS, smooth transitions, low current ripple (6.7%), and short settling time (0.32 s) are realized by using the proposed control method.

To verify transient response of the prototype, the results with changing output current references are given in Fig. 17. I_{o_ref} is

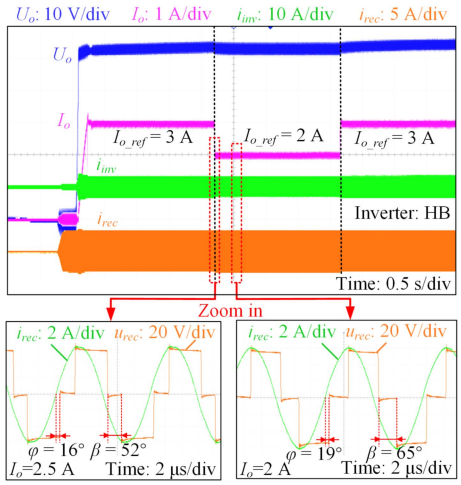

Fig. 17. Experimental waveforms with different I_{o_ref} during CC charging.

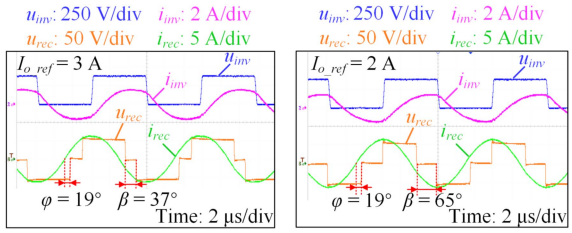

Fig. 18. Steady-state waveforms when (a) $I_{o\_ref} = 3$ A (b) $I_{o\_ref} = 2$ A.

TABLE II
MEASURED VALUES OF INPUT AND OUTPUT PARAMETERS

Parameters	Values
U_{in}	380 V
I_{in}	0.438 A
P_{in}	166 W
U_o	52.5 V
I_o	2.99 A
P_o	157 W
η	94.4%

changed from 3 A to 2 A, and then changed back to 3 A. It can be seen that the system can response rapidly to track I_{o_ref}. During the transition from 3 A to 2 A, a small deviation occurs between φ and its reference. For example, when the current is 2.5 A, φ is 16°, which is slightly lower than its reference value of 18°. Since φ remains above 0, the secondary-side full-bridge can still achieve ZVS. After the current stabilizes at the reference value of 2 A, φ also stabilizes at about 19°.

Fig. 18 shows the steady-state waveforms. As a result of the output-control loop, the duty cycle of u_{rec} is successfully adjusted according to I_{o_ref}. The value of β for $I_{o\_ref} = 3$ A is 37° and it changes to 65° when I_{o_ref} decreases to 2 A. Moreover, for both cases with two different I_{o_ref}, φ maintains stably at 19°, which is close to its reference value of 18°. This proves that the synchronization loop is also effective.

The measured DC–DC efficiency η of the prototype during CC charging at a 157 W output is 94.4%, as shown in Table II.

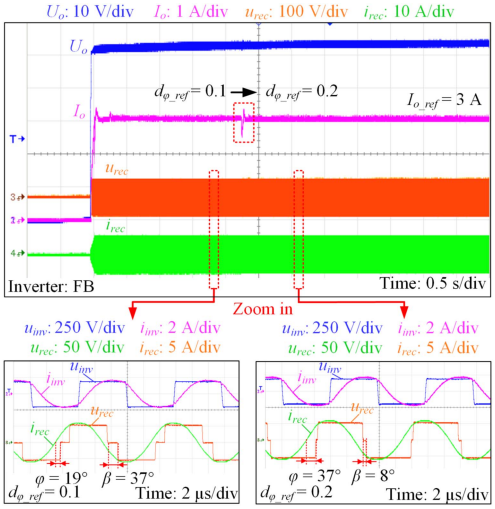

Fig. 19. Experimental waveforms with different d_{φ_ref} when $I_{o\_ref} = 3$ A.

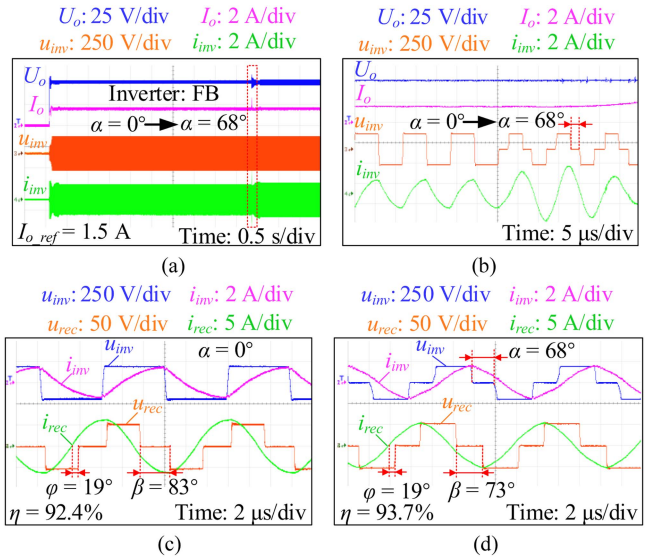

Fig. 20. Experimental waveforms with dual-side control when $I_{o\_ref} = 1.5$ A. (a) Complete waveforms. (b) Transition when α changes from 0° to 68°. (c) Steady-state waveforms when $\alpha = 0°$. (d) Steady-state waveforms when $\alpha = 68°$.

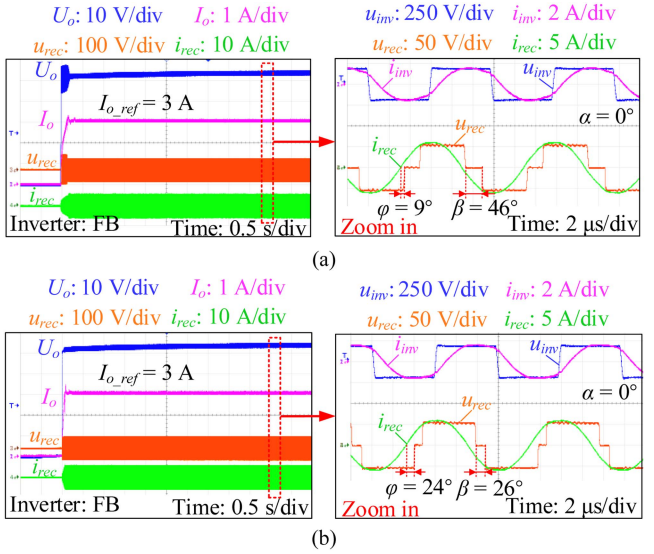

Fig. 21. Experimental waveforms with circuit parameter errors where: (a) $e_{Cp} = +5\%$, $e_{Cs} = +5\%$, and $e_M = +10\%$ (b) $e_{Cp} = +5\%$, $e_{Cs} = +5\%$, and $e_M = -10\%$.

Fig. 19 shows the performance of the prototype when d_{φ_ref} changes from 0.1 to 0.2. Based on (5), d_{β_ref} changes from 0.21 to 0.05 in response to the change in d_{φ_ref}, which increases the input error of the synchronization loop. As a result, the phase shift angle of the u_{rec} will increase and cause a temporary fluctuation in the output current I_o. However, under the control of the output loop, I_o remains stabilized at its reference value after the small fluctuation. φ eventually stabilizes at 37°, close to its reference value of 36°. β eventually stabilizes at 8°, close to its reference value of 9°. This indicates that the proposed control method effectively adjusts φ while maintaining the stability of the output current.

The proposed method is also applicable to a system with primary-side voltage regulation. For example, the equivalent output voltage of the primary-side inverter, i.e., U_{inv}, is adjusted by using the phase-shift control. According to (4) and (5), when the value of U_{inv} is changed by the primary-side controller, the new U_{inv} should be sent to the secondary-side controller for updating the value of d_{β_ref}. With the phase shift control, U_{inv} is adjusted as $U_{inv} = 4/\pi * U_{\text{in}} * \cos(\alpha/2)$, where α is the angle corresponding to the time interval when u_{inv} is 0 V. Based on (4) and (5), the reference value of β for $I_{o\_ref} = 1.5$ A, $d_{\varphi\_ref} = 0.1$ and $\alpha = 0°$ is 83°; it changes to 74° when α increases to 68°. The experimental waveforms of the prototype system with the proposed secondary-side control and also the primary-side phase-shift modulation when $I_{o\_ref} = 1.5$ A are shown in Fig. 20. According to Fig. 20, after α changes from 0° to 68°, φ remains at 19°, β changes from 83° to 73°, and I_o remains at 1.5 A, all of which are close to their reference values. In addition, the DC–DC efficiency increases from 92.4% to 93.7%. This experiment proves that the proposed method can perform well with the primary-side phase-shift modulation.

To test the robustness of the proposed methods, experiments are carried out with circuit parameter errors. The actual values of C_p and C_s are changed to 7.2 nF and 45 nF, respectively, to simulate the case where $e_{Cp} = +5\%$ and $e_{Cs} = +5\%$. Meanwhile the measured value M_{mea} is changed to 79.34 μH or 64.95 μH to simulate the case where $e_M = \pm 10\%$. The corresponding experimental waveforms are shown in Fig. 21.

It can be seen from Fig. 21 that the output current remains stable at its reference value, unaffected by the parameter errors. The steady state φ and β are basically consistent with the theoretical analysis in Fig. 8(a). The proposed control method can still work effectively when $e_{Cp} = +5\%$, $e_{Cs} = +5\%$, and $e_M = \pm 10\%$.

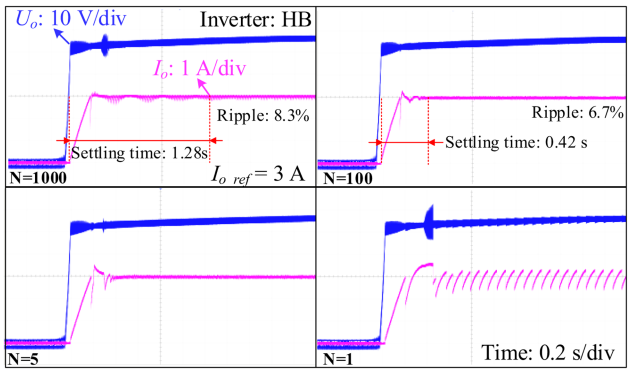

Fig. 22. Experimental waveforms with different N when $I_{o\_ref} = 3$ A.

Furthermore, the influence of different synchronization cycles ($N = 1000, 100, 5, 1$) on the control system are tested, and the corresponding experimental waveforms are shown in Fig. 22. It can be seen from Fig. 22 that when N increases from 100 to 1000, both the settling time and the current ripple increase. This is because with a larger N, the accumulated error of φ is larger when entering the synchronization loop. As a result, a larger phase shift of the rectifier input voltage occurs, consequently leading to an increase in current ripple. When N is less than 5, the system will oscillate because the synchronization loop and the output-control loop interfere with each other. In order to ensure system stability while also optimizing dynamic response, N is set to 15 in the prototype system.

It should be noted that the difference of the switching periods of the primary and secondary converters is 0.15 ns in this prototype due to the error in the oscillators of the MCUs. However, this error apparently does not affect the control of the system. The reason is that the accumulation speed of the phase difference between the secondary driving signals and the primary driving signals due to this oscillator frequency error is much slower than the changing speed of the phases of the secondary driving signals which are manipulated by the synchronization loop.

VI. Conclusion

In this article, a novel synchronous secondary-side control method without AC current detection and real-time wireless communication is proposed. The method includes an output-control loop and a synchronization loop. The output-control loop adjusts the output, either current or voltage, of the system by controlling the duty cycle of the rectifier input voltage. The synchronization loop realizes phase synchronization and ZVS by tracking the optimal phase of the rectifier input voltage. The small-signal model of the proposed system is built and used to design the controller parameters. The experiment results prove that the prototype system performs well with the proposed control method. The proposed method only requires sampling of the DC output information. Therefore, auxiliary hardware for AC current detection is not needed, and the cost and complexity of the system is reduced. Moreover, this novel method can avoid the drawback of susceptibility to high-frequency noise interference in AC current sampling.

Appendix

The calculation process of the small signal model is presented in this section. The inductor currents and capacitor voltages shown in Fig. 1 are selected as state variables. Based on Kirchhoff's laws, the SS WPT system can be described as

$$\begin{cases} L_p \frac{\mathrm{d}i_{inv}}{\mathrm{d}t} = u_{inv} - R_1 i_{inv} - u_{Cp} + M \frac{\mathrm{d}i_{rec}}{\mathrm{d}t} \\ C_p \frac{\mathrm{d}u_{Cp}}{\mathrm{d}t} = i_{inv} \\ L_s \frac{\mathrm{d}i_{rec}}{\mathrm{d}t} = M \frac{\mathrm{d}i_{inv}}{\mathrm{d}t} - R_2 i_{rec} - u_{Cs} - u_{rec} \\ C_s \frac{\mathrm{d}u_{Cs}}{\mathrm{d}t} = i_{rec} \\ C_f \frac{\mathrm{d}u_{Cf}}{\mathrm{d}t} = i_{o1} - i_o \\ L_f \frac{\mathrm{d}i_o}{\mathrm{d}t} = u_{Cf} - R_f i_o - U_o \end{cases} \tag{16}$$

where R_f is the equivalent parasitic resistance of the DC link.

Based on the GSSA method, a state variable $x(t)$ can be expressed as

$$x(t) = \langle x \rangle_s (t) \sin \omega t + \langle x \rangle_c (t) \cos \omega t \tag{17}$$

where $\langle x \rangle_s$ and $\langle x \rangle_c$ are the coefficients of the sine and cosine components of the Fourier expansion of $x(t)$.

Based on (17), all state variables can be expressed as

$$\begin{cases} u_{inv} = U_{inv} \sin \omega t \\ i_{inv} = x_1 \sin \omega t + x_2 \cos \omega t \\ u_{Cp} = x_3 \sin \omega t + x_4 \cos \omega t \\ i_{rec} = x_5 \sin \omega t + x_6 \cos \omega t \\ u_{Cs} = x_7 \sin \omega t + x_8 \cos \omega t \\ u_{Cf} = x_9 \\ i_o = x_{10} \end{cases} \tag{18}$$

where x_1 and x_2 are the coefficients of the sine and cosine components of the Fourier expansion of i_{inv}, x_3 and x_4 are the coefficients of the sine and cosine components of the Fourier expansion of u_{Cp}, and so forth.

Substituting (18) into (16), (16) can be rewritten as (19).

To deal with the nonlinear characteristics of the converters, the extended describing function (EDF) method is used to obtain the linearized model of the converter [29], [32]. Following the EDF method, the values of $\langle u_{rec} \rangle_s$, $\langle u_{rec} \rangle_c$, and i_{o1} are obtained by (20).

The large signal model of the system is given by (19) and (20). In order to establish a small signal model, the state variable x needs to be expressed as the sum of the steady-state X and disturbance $\hat{x}$, as shown in (21).

Substituting (21) into (19) and (20), and eliminating the steady-state values on both sides of the equal sign, the small signal model of the system is obtained. The steady-state values are selected as $I_o = 3$ A, $d_\varphi = 0.1$, and $d_\beta = 0.21$ based on (5).

$\langle \hat{u}_{rec} \rangle_s$, $\langle \hat{u}_{rec} \rangle_c$, and $\hat{i}_{o1}$ are linearized based on Taylor theorem, as shown in (22)

$$\begin{cases} L_p \frac{\mathrm{d}x_1}{\mathrm{d}t} - M \frac{\mathrm{d}x_5}{\mathrm{d}t} = U_{inv} - x_3 - R_1 x_1 + L_\mathrm{p} \omega x_2 - \omega M x_6 \\ L_p \frac{\mathrm{d}x_2}{\mathrm{d}t} - M \frac{\mathrm{d}x_6}{\mathrm{d}t} = -x_4 - R_1 x_2 - L_\mathrm{p} \omega x_1 + \omega M x_5 \\ C_p \frac{\mathrm{d}x_3}{\mathrm{d}t} = x_1 + C_p \omega x_4 \\ C_p \frac{\mathrm{d}x_4}{\mathrm{d}t} = x_2 - C_p \omega x_3 \\ L_s \frac{\mathrm{d}x_5}{\mathrm{d}t} - M \frac{\mathrm{d}x_1}{\mathrm{d}t} = -\omega M x_2 - R_2 x_5 + L_\mathrm{s} \omega x_6 - x_7 - \langle u_{rec} \rangle_s \\ L_s \frac{\mathrm{d}x_6}{\mathrm{d}t} - M \frac{\mathrm{d}x_2}{\mathrm{d}t} = \omega M x_1 - R_2 x_6 - L_\mathrm{s} \omega x_5 - x_8 - \langle u_{rec} \rangle_c \\ C_s \frac{\mathrm{d}x_7}{\mathrm{d}t} = x_5 + C_s \omega x_8 \\ C_s \frac{\mathrm{d}x_8}{\mathrm{d}t} = x_6 - C_s \omega x_7 \\ C_f \frac{\mathrm{d}x_9}{\mathrm{d}t} = i_{o1} - x_{10} \\ L_f \frac{\mathrm{d}x_{10}}{\mathrm{d}t} = x_9 - R_f x_{10} - U_o \end{cases} \tag{19}$$

$$\begin{cases} \langle u_{rec} \rangle_s = \frac{4}{\pi} x_9 \cos \frac{d_\beta \pi}{2} \frac{x_5}{\sqrt{{x_5}^2 + {x_6}^2}} \cos \left[\left(d_\varphi + \frac{d_\beta}{2} \right) \pi \right] \\ \qquad + \frac{4}{\pi} x_9 \cos \frac{d_\beta \pi}{2} \frac{x_6}{\sqrt{{x_5}^2 + {x_6}^2}} \sin \left[\left(d_\varphi + \frac{d_\beta}{2} \right) \pi \right] \\ \langle u_{rec} \rangle_c = -\frac{4}{\pi} x_9 \cos \frac{d_\beta \pi}{2} \frac{x_5}{\sqrt{{x_5}^2 + {x_6}^2}} \sin \left[\left(d_\varphi + \frac{d_\beta}{2} \right) \pi \right] \\ \qquad + \frac{4}{\pi} x_9 \cos \frac{d_\beta \pi}{2} \frac{x_6}{\sqrt{{x_5}^2 + {x_6}^2}} \cos \left[\left(d_\varphi + \frac{d_\beta}{2} \right) \pi \right] \\ i_{o1} = \frac{\sqrt{{x_5}^2 + {x_6}^2}}{\pi} \left[\cos \left(d_\varphi \pi \right) + \cos \left(d_\varphi \pi + d_\beta \pi \right) \right] \end{cases} \tag{20}$$

$$x = X + \hat{x} \tag{21}$$

$$\begin{cases} \langle \hat{u}_{rec} \rangle_s = \frac{\partial \langle u_{rec} \rangle_s}{\partial x_5} \hat{x}_5 + \frac{\partial \langle u_{rec} \rangle_s}{\partial x_6} \hat{x}_6 + \frac{\partial \langle u_{rec} \rangle_s}{\partial d_\beta} \hat{d}_\beta \\ \qquad + \frac{\partial \langle u_{rec} \rangle_s}{\partial d_\varphi} \hat{d}_\varphi + \frac{\partial \langle u_{rec} \rangle_s}{\partial x_9} \hat{x}_9 \\ \langle \hat{u}_{rec} \rangle_c = \frac{\partial \langle u_{rec} \rangle_c}{\partial x_5} \hat{x}_5 + \frac{\partial \langle u_{rec} \rangle_c}{\partial x_6} \hat{x}_6 + \frac{\partial \langle u_{rec} \rangle_c}{\partial d_\beta} \hat{d}_\beta \\ \qquad + \frac{\partial \langle u_{rec} \rangle_c}{\partial d_\varphi} \hat{d}_\varphi + \frac{\partial \langle u_{rec} \rangle_c}{\partial x_9} \hat{x}_9 \\ \hat{i}_{o1} = \frac{\partial \hat{i}_{o1}}{\partial x_5} \hat{x}_5 + \frac{\partial \hat{i}_{o1}}{\partial x_6} \hat{x}_6 + \frac{\partial \hat{i}_{o1}}{\partial d_\beta} \hat{d}_\beta + \frac{\partial \hat{i}_{o1}}{\partial d_\varphi} \hat{d}_\varphi. \end{cases} \tag{22}$$

Based on (2), the steady-state duty cycle d_β can be derived as

$$d_{\beta\_ss} = \frac{1}{\pi} \arccos \left[\frac{\pi I_{o\_ref}}{\sqrt{{x_5}^2 + {x_6}^2}} - \cos \left(d_\varphi \pi \right) \right] - d_\varphi. \tag{23}$$

According to (23), $\hat{d}_{\beta\_ss}$ is linearized as

$$\hat{d}_{\beta\_ss} = \frac{\partial d_{\beta\_ss}}{\partial x_5} \hat{x}_5 + \frac{\partial d_{\beta\_ss}}{\partial x_6} \hat{x}_6 + \frac{\partial d_{\beta\_ss}}{\partial d_\varphi} \hat{d}_\varphi. \tag{24}$$

The small signal state-space equation of the system is derived based on (19)–(24) as

$$\begin{cases} \dot{x} = Ax + Bu \\ y = Cx + Du \end{cases} \tag{25}$$

where x is the state variable vector containing the sine and cosine coefficients of currents and voltages, which is given by

$$x = [\hat{x}_1, \hat{x}_2, \hat{x}_3, \hat{x}_4, \hat{x}_5, \hat{x}_6, \hat{x}_7, \hat{x}_8, \hat{x}_9, \hat{x}_{10}]$$

u and y are input and output vectors, respectively, which are given by

$$\begin{aligned} u &= \left[\hat{d}_\beta, \hat{d}_\varphi \right] \\ y &= \left[\hat{i}_o, \hat{d}_{\beta\_ss} \right] \\ &= \left[\hat{x}_{10}, \left[\frac{\partial d_{\beta\_ss}}{\partial x_5}, \frac{\partial d_{\beta\_ss}}{\partial x_6} \right] [\hat{x}_5, \hat{x}_6]^T + \frac{\partial d_{\beta\_ss}}{\partial d_\varphi} \hat{d}_\varphi \right]. \end{aligned}$$

The expressions of A, B, C, and D are matrixes related to system parameters, which can be obtained from (24) and (26)

$$\begin{cases} L_p \frac{\mathrm{d}\hat{x}_1}{\mathrm{d}t} - M \frac{\mathrm{d}\hat{x}_5}{\mathrm{d}t} = -\hat{x}_3 - R_1 \hat{x}_1 + L_\mathrm{p} \omega \hat{x}_2 - \omega M \hat{x}_6 \\ L_p \frac{\mathrm{d}\hat{x}_2}{\mathrm{d}t} - M \frac{\mathrm{d}\hat{x}_6}{\mathrm{d}t} = -x_4 - R_1 \hat{x}_2 - L_\mathrm{p} \omega \hat{x}_1 + \omega M \hat{x}_5 \\ C_p \frac{\mathrm{d}\hat{x}_3}{\mathrm{d}t} = \hat{x}_1 + C_p \omega \hat{x}_4 \\ C_p \frac{\mathrm{d}\hat{x}_4}{\mathrm{d}t} = \hat{x}_2 - C_p \omega \hat{x}_3 \\ L_s \frac{\mathrm{d}\hat{x}_5}{\mathrm{d}t} - M \frac{\mathrm{d}\hat{x}_1}{\mathrm{d}t} = -\omega M \hat{x}_2 - R_2 \hat{x}_5 + L_s \omega \hat{x}_6 - \hat{x}_7 - \langle \hat{u}_{rec} \rangle_s \\ L_s \frac{\mathrm{d}\hat{x}_6}{\mathrm{d}t} - M \frac{\mathrm{d}\hat{x}_2}{\mathrm{d}t} = \omega M \hat{x}_1 - R_2 \hat{x}_6 - L_s \omega \hat{x}_5 - \hat{x}_8 - \langle \hat{u}_{rec} \rangle_c \\ C_s \frac{\mathrm{d}\hat{x}_7}{\mathrm{d}t} = \hat{x}_5 + C_s \omega \hat{x}_8 \\ C_s \frac{\mathrm{d}\hat{x}_8}{\mathrm{d}t} = \hat{x}_6 - C_s \omega \hat{x}_7 \\ C_f \frac{\mathrm{d}\hat{x}_9}{\mathrm{d}t} = \frac{\partial \hat{i}_{o1}}{\partial x_5} \hat{x}_5 + \frac{\partial \hat{i}_{o1}}{\partial x_6} \hat{x}_6 + \left[\frac{\partial \hat{i}_{o1}}{\partial d_\beta}, \frac{\partial \hat{i}_{o1}}{\partial d_\varphi} \right] u^T - \hat{i}_o \\ L_f \frac{\mathrm{d}\hat{i}_o}{\mathrm{d}t} = \hat{x}_9 - R_f \hat{i}_o \end{cases} \tag{26}$$

where

$$\begin{aligned} \langle \hat{u}_{rec} \rangle_s &= \frac{\partial \langle u_{rec} \rangle_s}{\partial x_5} \hat{x}_5 + \frac{\partial \langle u_{rec} \rangle_s}{\partial x_6} \hat{x}_6 + \frac{\partial \langle u_{rec} \rangle_s}{\partial x_9} \hat{x}_9 \\ &\quad + \left[\frac{\partial \langle u_{rec} \rangle_s}{\partial d_\beta}, \frac{\partial \langle u_{rec} \rangle_s}{\partial d_\varphi} \right] u^T \\ \langle \hat{u}_{rec} \rangle_c &= \frac{\partial \langle u_{rec} \rangle_c}{\partial x_5} \hat{x}_5 + \frac{\partial \langle u_{rec} \rangle_c}{\partial x_6} \hat{x}_6 + \frac{\partial \langle u_{rec} \rangle_c}{\partial x_9} \hat{x}_9 \\ &\quad + \left[\frac{\partial \langle u_{rec} \rangle_c}{\partial d_\beta}, \frac{\partial \langle u_{rec} \rangle_c}{\partial d_\varphi} \right] u^T. \end{aligned}$$

The transfer functions can be calculated by

$$\left[G_{d_\varphi}(s), G_{d_\beta}(s), G_{d_{\varphi\beta}}(s) \right] = C(sI - A)^{-1} B + D. \tag{27}$$

REFERENCES

[1] "Delay comparison between bluetooth HC-05 and NRF24l01," Accessed: May 28, 2019. [Online]. Available: https://www.researchgate.net/figure/Delay-comparison-between-Bluetooth-HC-05-anda-NRF24l01_tbl1_333432620

[2] J. Malhotra, "ZigBee technology: Current status and future scope," in *Proc. Int. Conf. Comput. Comput. Sci.*, 2015, pp. 163–169.

[3] *IEEE Approved Draft Standard for Information Technology – Telecommunications and Information Exchange Between Systems Local and Metropolitan Area Networks – Specific Requirements - Part 11: Wireless Local Area Network (LAN) Medium Access Control (MAC) and Physical Layer (PHY) Specifications,*, IEEE P802.11-REVme/D7.0, 2024.

[4] D. J. Thrimawithana, U. K. Madawala, and M. Neath, "A synchronization technique for bidirectional IPT systems," *IEEE Trans. Power Electron.*, vol. 60, no. 1, pp. 301–309, Jan. 2013.

[5] R. Mai, Y. Liu, Y. Li, P. Yue, G. Cao, and Z. He, "An active-rectifier-based maximum efficiency tracking method using an additional measurement coil for wireless power transfer," *IEEE Trans. Power Electron.*, vol. 33, no. 1, pp. 716–728, Jan. 2018.

[6] Y. Zhang, S. Chen, X. Li, and Y. Tang, "Dual-side phase-shift control of wireless power transfer implemented on primary side based on driving windings," *IEEE Trans. Ind. Electron.*, vol. 68, no. 9, pp. 8999–9002, Sep. 2021.

[7] Y. Zhang, X. Li, S. Chen, and Y. Tang, "Soft switching for strongly coupled wireless power transfer system with 90° dual-side phase shift," *IEEE Trans. Ind. Electron.*, vol. 69, no. 1, pp. 282–292, Jan. 2022.
[8] Y. Tang, Y. Chen, U. K. Madawala, D. J. Thrimawithana, and H. Ma, "A new controller for bidirectional wireless power transfer systems," *IEEE Trans. Power Electron.*, vol. 33, no. 10, pp. 9076–9087, Oct. 2018.
[9] D. J. Thrimawithana, U. K. Madawala, and M. Neath, "A P&Q based synchronization technique for Bi-directional IPT pick-ups," in *Proc. IEEE 9th Int. Conf. Power Electron. Drive Syst.*, 2011, pp. 40–45.
[10] X. Liu, N. Jin, D. Ma, and X. Yang, "A simple and effective synchronization technique for wireless power transfer system," in *Proc. IEEE Wireless Power Transfer Conf.*, 2018, pp. 1–4.
[11] K. Colak, E. Asa, M. Bojarski, D. Czarkowski, and O. C. Onar, "A novel phase-shift control of semibridgeless active rectifier for wireless power transfer," *IEEE Trans. Power Electron.*, vol. 30, no. 11, pp. 6288–6297, Nov. 2015.
[12] S. Ann and B. K. Lee, "Analysis of impedance tuning control and synchronous switching technique for a semibridgeless active rectifier in inductive power transfer systems for electric vehicles," *IEEE Trans. Power Electron.*, vol. 36, no. 8, pp. 8786–8798, Aug. 2021.
[13] D. Zhang, M. Chen, B. Li, X. Wang, X. Sun, and F. Jiang, "Synchronization strategy based on resonant current detection for bidirectional wireless charging system," *IEEE Trans. Power Electron.*, vol. 37, no. 9, pp. 11436–11449, Sep. 2022.
[14] S. Jia, C. Chen, P. Liu, and S. Duan, "A digital phase synchronization method for bidirectional inductive power transfer," *IEEE Trans. Ind. Electron.*, vol. 67, no. 8, pp. 6450–6460, Aug. 2020.
[15] R. K. Yakala, D. Nayak, and S. Pramanick, "Input reactive power control of bidirectional WPT to improve system efficiency," *IEEE Trans. Ind. Appl.*, vol. 60, no. 4, pp. 5813–5824, Jul./Aug. 2024.
[16] Y. Jiang et al., "Phase-locked loop combined with chained trigger mode used for impedance matching in wireless high power transfer," *IEEE Trans. Power Electron.*, vol. 35, no. 4, pp. 4272–4285, Apr. 2020.
[17] S. Cochran and D. Costinett, "Frequency synchronization and control for a 6.78 MHz WPT active rectifier," in *Proc. IEEE 19th Workshop Control Model. Power Electron.*, 2018, pp. 1–7.
[18] H. Li, L. Tan, H. Qi, X. Li, Z. Wu, and X. Huang, "Research on secondary-side synchronization method of wireless power transfer systems," in *Proc. 49th Annu. Conf. IEEE Ind. Electron. Soc.*, 2023, pp. 1–6.
[19] T. Tan, K. Chen, Y. Jiang, Q. Lin, L. Yuan, and Z. Zhao, "A bidirectional wireless power transfer system control strategy independent of real-time wireless communication," *IEEE Trans. Ind. Appl.*, vol. 56, no. 2, pp. 1587–1598, Mar.-Apr. 2020.
[20] F. Liu, K. Li, K. Chen, and Z. Zhao, "A phase synchronization technique based on perturbation and observation for bidirectional wireless power transfer system," *IEEE J. Emerg. Sel. Topics Power Electron.*, vol. 8, no. 2, pp. 1287–1297, Jun. 2020.
[21] D. Shirasaki, T. Fujita, and H. Fujimoto, "Novel synchronous rectification and receiving power compensation method for WPT only by DC current sensor," *IEEE J. Emerg. Sel. Topics Ind. Electron.*, vol. 3, no. 4, pp. 1159–1167, Oct. 2022.
[22] X. Zhang et al., "A control strategy for efficiency optimization and wide ZVS operation range in bidirectional inductive power transfer system," *IEEE Trans. Ind. Electron.*, vol. 66, no. 8, pp. 5958–5969, Aug. 2019.
[23] Y. Liu, U. K. Madawala, R. Mai, and Z. He, "An optimal multivariable control strategy for inductive power transfer systems to improve efficiency," *IEEE Trans. Power Electron.*, vol. 35, no. 9, pp. 8998–9010, Sep. 2020.
[24] M. Li, J. Deng, D. Chen, W. Wang, and Z. Wang, "Maximum efficiency tracking and ZVS realization for wide output voltage range employing segmented TPS modulation scheme," *IEEE Trans. Veh. Technol.*, vol. 72, no. 10, pp. 12770–12783, Oct. 2023.
[25] H. Li, J. Xu, F. Gao, Y. Zhang, X. Yang, and H. Tang, "Duty cycle control strategy for dual-side LCC resonant converter in wireless power transfer systems," *IEEE Trans. Transp. Electrific.*, vol. 8, no. 2, pp. 1944–1955, Jun. 2022.
[26] W. Zhang, S.-C. Wong, C. K. Tse, and Q. Chen, "Design for efficiency optimization and voltage controllability of series–series compensated inductive power transfer systems," *IEEE Trans. Power Electron.*, vol. 29, no. 1, pp. 191–200, Jan. 2014.
[27] S. Li, W. Li, J. Deng, T. D. Nguyen, and C. C. Mi, "A double-sided LCC compensation network and its tuning method for wireless power transfer," *IEEE Trans. Veh. Technol.*, vol. 64, no. 6, pp. 2261–2273, Jun. 2015.
[28] Y. Zhang, L. Wang, S. Li, C. Tao, and Z. Liu, "Parameter estimation of wireless power transfer systems based on the DC input voltage and current," in *Proc. Wireless Power Week*, 2022, pp. 318–321.
[29] Z. U. Zahid, Z. Dalala, and J.-S. J. Lai, "Small-signal modeling of series-series compensated induction power transfer system," in *Proc. IEEE Appl. Power Electron. Conf. Expo.*, 2014, pp. 2847–2853.
[30] S. R. Sanders, J. M. Noworolski, X. Z. Liu, and G. C. Verghese, "Generalized averaging method for power conversion circuits," *IEEE Trans. Power Electron.*, vol. 6, no. 2, pp. 251–259, Apr. 1991.
[31] K. Ogata, *Discrete-Time Control Systems*, 2nd ed. Englewood Cliffs, NJ, USA: Prentice-Hall, 1995.
[32] E. X.-Q. Yang, "Extended describing function method for small-signal modeling of resonant and multi-resonant converters," Ph.D. dissertation, Dept. Elect. Eng., Virginia Tech., Blacksburg, VA, USA, 1994.

Kangxing Zheng was born in Zhejiang Province, China, in 1998. He received the B.Eng. degree in electrical engineering and its automation from the Harbin Institute of Technology, Harbin, China, in 2020. He is currently working toward the Ph.D. degree in electrical engineering with the College of Electrical Engineering, Zhejiang University, Hangzhou, China.

His current research interests include wireless power transfer technologies and power electronics.

Jingzhi Ren received the B.Eng. degree from the Shandong University, Jinan, China, in 2019, and the M.S. degree from the Zhejiang University, Hangzhou, China, in 2022, both in electrical engineering.

He is currently a Senior Engineer with Ningbo Douch Power Technology Co., Ltd., Ningbo, China. His current research interests include wireless power transfer technologies and power electronics.

Wenxing Zhong (Senior Member, IEEE) received the B.Eng. degree in electrical engineering from Tsinghua University, Beijing, China, in 2007, and the Ph.D. degree in electrical engineering from the City University of Hong Kong, Hong Kong, in 2012. He is currently a Professor with the Faculty of Electrical Engineering and Computer Science, Ningbo University, Zhejiang, China. From 2016 to 2017, he was a Research Assistant Professor with the Department of Electrical and Electronic Engineering, University of Hong Kong, Hong Kong. From 2017 to 2024, he was a Professor with Zhejiang University. His research interests include wireless power transfer and power electronics.

Dr. Zhong was the recipient of the Transactions on Power Electronics First Prize Paper Award in 2015 and 2016, respectively.